Volume 25
Number 4
28 January 2023
Pages 2645–3552

PCCP

Physical Chemistry Chemical Physics

rsc.li/pccp

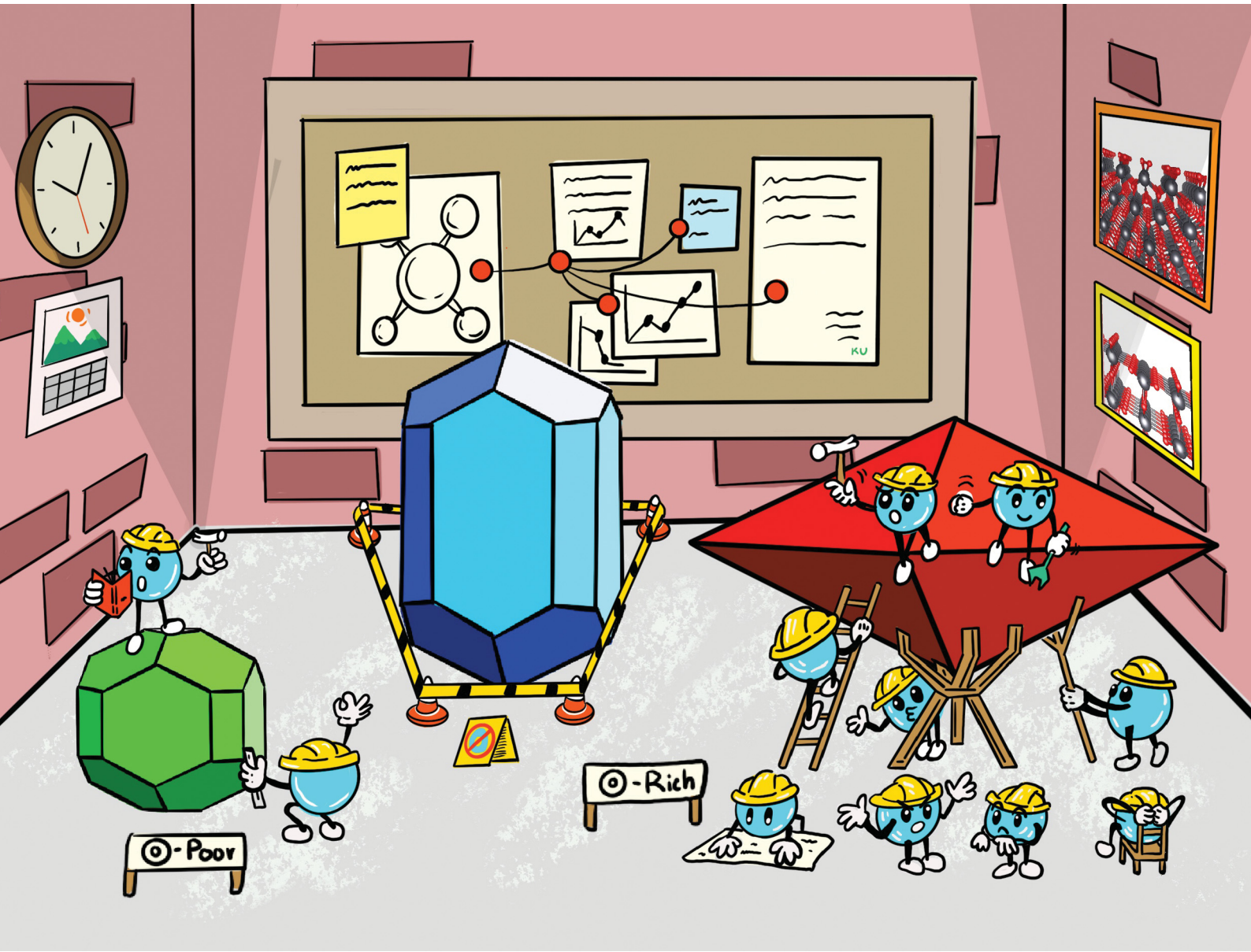

ISSN 1463-9076

ROYAL SOCIETY OF CHEMISTRY

PAPER

Pakpoom Reunchan *et al.*

Effects of oxygen pressure on the morphology and surface energetics of β-PbO_2: insight from DFT calculations

PCCP

ROYAL SOCIETY OF CHEMISTRY

PAPER

Cite this: *Phys. Chem. Chem. Phys.*, 2023, **25**, 2793

Effects of oxygen pressure on the morphology and surface energetics of β-PbO_2: insight from DFT calculations†

Aroon Ananchuensook,[a] Chatchawal Wongchoosuk,[a] Jiraroj T-Thienprasert,[a] Adisak Boonchun,[a] Sirichok Jungthawan[b] and Pakpoom Reunchan *[a]

Received 4th October 2022,
Accepted 6th December 2022

DOI: 10.1039/d2cp04632f

rsc.li/pccp

For over a century, lead dioxide (PbO_2) has been investigated in lead–acid batteries and extensively utilized in a variety of applications. Identifying the surface properties and equilibrium morphology of β-PbO_2 (rutile phase) particles is mandatory for industrial utilization and surface engineering. Using density-functional calculations within the generalized gradient approximation revised for solids (PBEsol), we investigate a variety of surface properties of β-PbO_2. The surface energies of low-Miller-index stoichiometric surfaces are firstly determined, and the (110) surface is found to be the most thermodynamically stable. The relative energetics of these surfaces are represented by a Wulff construction which shows an acicular shape, mostly dominated by the (110) and (100) surfaces. Besides, we investigate the surface chemistry of β-PbO_2 under reduction and oxidation conditions as a function of oxygen pressure, finding that most surfaces except for (100) and (110) are likely to be oxidized. Under oxygen pressure at 1 atm and oxygen-rich limit, the (101) surface is the most thermodynamically stable, dominating the Wulff construction with pyramidal shapes. Our results indicate that the growth conditions that cause non-stoichiometry of the surface could modify the equilibrium Wulff shape of β-PbO_2. Our predicted Wulff shapes and dominant facets agree with the experimental results in which the pyramidal shape of the β-PbO_2 grains has often been observed with the (101) preferred orientation.

1. Introduction

Since most metals are easily oxidized in the ambient atmosphere, it is often the case that metal-oxide surfaces are of interest rather than the metal itself. The properties of these surfaces have been the subject of practical investigations due to their utility in a variety of applications, including photocatalytic degradation,[1] gas sensing,[2] catalysis,[3] coatings,[4] optoelectronics,[5] and photovoltaics.[6] Since the discovery of lead–acid batteries, lead dioxide (PbO_2) has become of great importance due to its utility in various applications. Electrodes made from β-PbO_2 have been extensively investigated owing to their high electrical conductivity, strong oxidizing ability, facile fabrication feasibility, electrochemical stability, and low cost of production.[7–10] These features draw much interest to PbO_2 electrodes, and thus, many studies on amending their performance have been reported. For instance, the effects of doping with rare-earth elements, including Co,[11] Ce, Er, Gd, and La, on the properties of PbO_2 electrodes were investigated.[7] Composite electrodes based on β-PbO_2, *e.g.*, Co_3O_4/β-PbO_2/Ti electrodes, have also been developed to enhance the electrocatalytic performance and coating stability.[12] Furthermore, applications of PbO_2 as electrodes in hybrid supercapacitors have been studied.[13] Besides, β-PbO_2 has been known to be characterized by a combination of high electrical conductivity and high transparency although the band gap is somewhat narrow ($\ll 3$ eV) and is known as a narrow band gap transparent conducting oxide (NB-TCO);[14] owing to the Moss-Burstein effect a blue-shift of the optical band gap is observed when NB-TCO is donor doped to high concentrations.[5] This widely opens the opportunity to utilize PbO_2 in the field of optoelectronics similar to CdO.

In practice, PbO_2 nanoparticles were synthesized on substrates for utilization as electrodes in particular anodes. In addition to the crystalline phase, particle size and intrinsic factors such as defects, crystal morphology, and thereby particle shapes can highly affect the desirable properties and performance of PbO_2-based electrodes. This is because the electron or hole transfer, which impacts the electrode efficiency, is very sensitive to the surface atomic structures. The control of the crystal facet and particle shape is therefore as

[a] *Department of Physics, Faculty of Science, Kasetsart University, Bangkok 10900, Thailand. E-mail: pakpoom.r@ku.ac.th*

[b] *School of Physics, Institute of Science, Suranaree University of Technology, Nakhon Ratchasima, 30000, Thailand*

† Electronic supplementary information (ESI) available: The effects of spin–orbit coupling, formation enthalpies of metal oxides and atomic configurations of non-stoichiometric surfaces. See DOI: https://doi.org/10.1039/d2cp04632f

important as particle size and defect control.[15,16] For this reason, many investigations in various synthesis processes including electrochemical methods[17] and electrodeposition,[10,18–20] which aim to increase the performance of PbO_2 electrodes and nanostructures through the control of crystal morphology and facet, have been carried out. In thermodynamic equilibrium, the crystal shape can be determined through the Wulff construction using the surface energies of all facets. The estimation of surface energy is, thus, a key to optimizing the compositions of the Wulff (crystal) shape. Density-functional theory (DFT) calculations have become a well-established tool for the investigation of metal oxide surfaces.[21,22] This has motivated research in theoretical calculations of surface energies of many functional metal oxides, including oxides with a rutile crystal structure. The energetics of rutile TiO_2 surfaces have been extensively studied, and the (110) surface has been theoretically identified as the most stable surface with the lowest surface energy.[23–25] The calculated surface energies of stoichiometric SnO_2[26] and VO_2[27] in the rutile phase were also reported. Using these calculated surface energies, the Wulff shapes of stoichiometric rutile TiO_2 and VO_2 were proposed and discussed in comparison with the experiments.[27,28] Much attention is paid to the theoretical investigation of the nature of bulk β-PbO_2, including electronic structures,[29–31] the relativistic effect,[32] point defects, and their effect on electrical conductivity.[5,14] However, few works have been devoted to investigating the surfaces of β-PbO_2.[33–35] Regardless of its analogous structure to other rutile oxides, to our knowledge, only a recent study has reported its stoichiometric surface energies.[35] Gaining insight into the energetics and atomic geometries of the free surfaces including the Wulff shape is an important step to develop β-PbO_2-based devices.

This article presents the energetics and relative stability of low Miller-index surfaces of β-PbO_2 through DFT calculations within the Perdew–Burke–Ernzerhof functional revised for solids (PBEsol). Our investigation starts from the stoichiometric surfaces of β-PbO_2. Using the calculated surface energies, the thermodynamic equilibrium shape of stoichiometric β-PbO_2 is predicted through a Wulff construction which represents the relative energetics of these surfaces. We further investigate the redox properties of these low Miller index surfaces and subsequently calculate the surface energies of possible non-stoichiometric compositions of PbO_2 as a function of oxygen chemical potential. Taking the surface redox properties into account, the thermodynamic equilibrium morphologies of a PbO_2 particle are presented through Wulff construction at various oxygen partial pressures and temperatures. We find that the (101) plane somewhat dominates the equilibrium Wulff shapes, under ambient and O-rich conditions. The predicted pyramidal Wulff shape by our calculations may explain the experimental observation of the morphology of the β-PbO_2 crystallites.

2. Computational methods

Our DFT calculations were performed using the generalized-gradient approximation (GGA) of the Perdew–Burke–Ernzerhof revised for solids functional (PBEsol)[36] and the projector-augmented wave (PAW) method[37] to describe the interactions between the core and the valence electrons as implemented in the VASP code.[38] The Pb $6s^2 5d^{10} 6p^2$ and O $2s^2 2p^4$ electrons were treated as valence electrons. The energy cutoff of 400 eV was used for the planewave expansion, and a $9 \times 9 \times 9$ Monkhorst–Pack mesh[39] of the special *k*-point set was used for the bulk β-PbO_2 unit cell calculations. The use of these parameters was chosen to ensure the convergence of the bulk β-PbO_2 total energy. The calculated bulk fundamental properties, *i.e.*, lattice constant and enthalpy of formation, are in good agreement with measured values as shown in Table 1. It is known that local and semi-local functionals such as the local density approximation (LDA) and the GGA underestimate band gaps for most metal oxides. We find that the PBEsol predicts β-PbO_2 to be a metallic material with an overlap of 0.69 eV of the valence band maximum and conduction band minimum, similar to the previously reported value. This contrasts with the experimental measurement which reported β-PbO_2 to be a semiconductor with a fundamental band gap of ∼0.6 eV.[40] The mixing of exchange in the PBE functional with screened Hartree–Fock (HF) exchange as proposed by Heyd, Scuseria, and Ernzerhof in the HSE06 hybrid functional,[41] however, recovers the semiconducting property of β-PbO_2. It was found that the use of 25% of the HF exchange predicts β-PbO_2 to be a semiconductor with a direct band gap of 0.35 eV.[14] To reproduce the experimental band gap of ∼0.6 eV, based on our calculations, 31.5% of the HF exchange is required. The HSE06 yields lattice constant in very good agreement with the experimental lattice constant of less than 1% while the PBEsol slightly overestimates the experimental lattice constants by ∼1%. The calculated formation enthalpy within the PBEsol is very close to the experimental value compared to the HSE06 (Table 1). This indicates that PBEsol can capture most of the chemical and physical properties related to the Pb–O bonding. The surface energies, mostly involving the bond-breaking formation energy, are expected to be justified within the PBEsol. Our test calculations of the stoichiometric surface energies of β-PbO_2 show that the difference between the surface energies calculated using the HSE06 and PBEsol is ∼6%. All results reported in this article are therefore calculated within the PBEsol. Note that the inclusion of spin–orbit coupling is unlikely to affect the surface energies and thereby the Wulff shapes (see ESI†).

Table 1 Calculated structural parameters and formation enthalpies for β-PbO_2 and PbO. Experimental values are also listed

Material	Property	PBEsol	HSE06	Experiment
β-PbO_2	a (Å)	5.01	4.96	4.95–4.96[8,14]
	c (Å)	3.41	3.35	3.38[8,14]
	ΔH_f (eV)	−2.80	−2.47	−2.84[64]
β-PbO	a (Å)	5.92	5.87	5.89[65]
	b (Å)	5.54	5.49	5.49[65]
	c (Å)	4.71	4.67	4.75[65]
	ΔH_f (eV)	−2.28	−2.68	−2.26[65]

The unrelaxed surface structures are constructed from the relaxed bulk primitive cell of β-PbO_2. Here, we consider only the low Miller-index surfaces (110), (010), (001), (011), and (111) as they tend to be more stable compared to high Miller-index surfaces. First, the slab models of a surface were stoichiometrically built with thicknesses between 9 and 20 Å, depending on the Miller index of the respective surface. The thickness of the vacuum layer supercells is set to ∼15 Å. Test calculations show that the thicknesses of these slabs and vacuum layers are reasonably sufficient to give a converged surface energy. Both sides of the slab are geometrically equivalent to avoid the formation of electrical dipole moments, which can undesirably affect the surface energies. The cell parameters of the slab supercells are kept fixed throughout the calculations. Only atoms near the surfaces of the slab supercells are fully relaxed until the residual forces <0.02 eV Å^{-1}. The atoms in the inner part of the slab supercell are frozen to mimic the bulk region of β-PbO_2. The surface energy can be calculated by taking the difference between the total energies of a slab and the equivalent PbO_2 formula unit of the bulk and dividing by the total surface area (2A) of the slab:

$$\gamma = \frac{E_{\text{slab}} - nE_{\text{bulk}}}{2A}, \tag{1}$$

where E_{slab} is the total energy of the slab supercell containing n formula unit of bulk PbO_2 and E_{bulk} is the total energy per formula unit of bulk PbO_2. For instance, the (110) slab supercell, which is composed of 12 atoms of Pb and 24 atoms of O, contains 36/3 = 12 formula unit cells of bulk PbO_2 (n = 12).

We further investigate the stability of reduced and oxidized surfaces by calculating the free surface energy of non-stoichiometric surfaces. The thermodynamics approach to calculate the surface free energy of the non-stoichiometric surface was first proposed by Scheffler and Reuter[21] and has been successfully employed in many surface systems,[27,42,43]

$$\gamma(T,p) = \frac{E_{\text{slab}} - nE_{\text{bulk}} + \sum_i N_i\mu_i(T,p)}{2A}, \tag{2}$$

where N_i represents the number of extra or absent atoms of species i that are taken from or added to a reservoir with energy μ_i. To simulate a non-stoichiometric surface, the oxygen atoms are symmetrically removed or added to both sides of the surface slab. This is to ensure the similarity of the two surfaces and avoid spurious effects due to dipole formation. Therefore, the surface free energy for a non-stoichiometric surface (i = oxygen, O) can be written as

$$\gamma(T,p) = \frac{E_{\text{slab}} - nE_{\text{bulk}}}{2A} - \frac{N_{\text{O}}}{A}\mu_{\text{O}}(T,p), \tag{3}$$

where N_{O} is the number of absent ($N_{\text{O}} < 0$) or excess ($N_{\text{O}} > 0$) oxygen atoms and μ_{O} is the energy of the oxygen reservoir which is referenced as the total energy per atom of an isolate oxygen molecule, $\mu_{\text{O}}(T,p) = \tilde{\mu}_{\text{O}}(T,p) + \frac{1}{2}E_{\text{O}_2}$. Following a thermodynamic approach described in ref. 21, the oxygen chemical potential $\tilde{\mu}_{\text{O}}(T,p)$ is related to a given temperature T and pressure p by

$$\tilde{\mu}_{\text{O}}(T,p) = \tilde{\mu}_{\text{O}}(T,p_0) + \frac{1}{2}k_{\text{B}}T\ln\left(\frac{p}{p_0}\right), \tag{4}$$

where $\tilde{\mu}_{\text{O}}(T,p_0)$ is the half of the difference between Gibbs free energy per an O_2 molecule between 0 K and T at p_0 = 1 atm, indicating the oxygen chemical potential at a given temperature T and the standard pressure p_0 = 1 atm. Experimentally, $\tilde{\mu}_{\text{O}}$ can be varied depending on the growth or annealing processes but is constrained with bounds. Under thermodynamic equilibrium, the chemical potentials $\tilde{\mu}_{\text{Pb}}$ and $\tilde{\mu}_{\text{O}}$ must satisfy the stability condition, $\tilde{\mu}_{\text{Pb}} + 2\tilde{\mu}_{\text{O}} = \Delta H_{\text{f}}(PbO_2)$, where $\Delta H_{\text{f}}(PbO_2)$ is the formation enthalpy of PbO_2. For the oxygen-rich limit $\tilde{\mu}_{\text{O}} = 0$, the chemical potential of Pb is given by $\Delta H_{\text{f}}(PbO_2)$. For the oxygen-poor limit $\tilde{\mu}_{\text{O}}$ and $\tilde{\mu}_{\text{Pb}}$ are bound by the formation of PbO; $\tilde{\mu}_{\text{Pb}} + \tilde{\mu}_{\text{O}} < \Delta H_{\text{f}}(PbO)$ where $\Delta H_{\text{f}}(PbO)$ is the formation enthalpy of PbO. The formation enthalpies calculated using the PBEsol functional are $\Delta H_{\text{f}}(PbO_2) = -2.80$ eV and $\Delta H_{\text{f}}(PbO) = -2.28$ eV which are in good agreement with the experimental values of -2.84 eV and -2.26 eV, respectively. The accessible range of $\tilde{\mu}_{\text{O}}$ given by these conditions is between 0 (O-rich) and -0.46 eV (O-poor) which can be expressed as a function of pressure for a certain growth temperature using eqn (4). The surface free energies of the non-stoichiometric PbO_2 surface can then be estimated as a function of oxygen chemical potential and thereby pressure of gaseous oxygen. The shape of a stoichiometric crystal in its thermodynamic equilibrium is determined by the surface energies through the Wulff construction,[44] which is also used to model the crystal shape at different growth temperatures and O_2 pressures.

3. Results and discussion

A. Stoichiometric surfaces

First, the energetics of stoichiometric low-index surfaces of β-PbO_2 are investigated. The calculated surface energies of stoichiometric (110), (010), (001), (011), and (111) surfaces are listed in Table 2. The surface energies obtained from unrelaxed ($\gamma_{\text{unrelaxed}}$) and relaxed ($\gamma_{\text{relaxed}}$) slab supercells as well as the atomic coordination are also presented. We find that our calculated surface energies (γ_{relaxed}) are much smaller than recently reported surface energies of β-PbO_2.[35] Note that this is the first time the (111) surface energy of β-PbO_2 is reported.

Table 2 Calculated unrelaxed ($\gamma_{\text{unrelaxed}}$) and relaxed ($\gamma_{\text{relaxed}}$) surface energies for the low-index surfaces of β-PbO_2. The relaxed surface energies obtained by HSE are also listed in parentheses. $\Delta\gamma = \gamma_{\text{unrelaxed}} - \gamma_{\text{relaxed}}$

Surface	Pb coordination	O coordination	$\gamma_{\text{unrelaxed}}$ (J m^{-2})	γ_{relaxed} (J m^{-2})	$\Delta\gamma$ (J m^{-2})
110	5, 6	2, 3	0.93	0.72(0.65)	0.21
100	5	2	0.99	0.83(0.76)	0.16
101	5	2, 3	1.27	1.03(0.89)	0.24
001	4	2	1.46	1.33(1.24)	0.13
111	4, 5	2	1.79	1.44(1.47)	0.35

Much higher surface energies reported in ref. 35 than those reported in the present work are possibly due to the electronic structure calculation approach, pseudopotentials, or modelling of slab supercells. We have verified our methodology by calculating the surface energy of rutile TiO_2 in the (110) orientation, yielding a surface energy of 0.53 J m^{-2} which is in excellent agreement with the previously reported values, ranging between 0.48 and 0.53 J m^{-2} based on the PBE.[45,46] Note that the use of the DFT-LDA or the HF approach apparently resulted in sizable surface energies for rutile and anatase TiO_2, compared with the PBE functional.[23,46] Furthermore, our calculated surface energies are well comparable with those reported for isostructural rutile TiO_2,[23] SnO_2,[47] and VO_2.[27]

As summarized in Table 2, the (110) surface is the most energetically stable for rutile TiO_2,[23] SnO_2,[47] and VO_2.[27] The next most energetically stable surface is the (100) surface, followed by (101), (001), and (111) surfaces, respectively; the surface energies of these orientations are (110) < (100) < (101) < (001) < (111) as for rutile VO_2. This order of the surface energies can be expected from the coordination of the surface atoms and noticeably remains unchanged regardless of the atomic relaxations of the slab models.

As shown in Fig. 1(a), the (110) surface terminates in bridging-O atoms; an O atom bonds with two Pb atoms along the [001] direction. An O atom in the lower lying in-plane O atoms bonds with three Pb atoms which are five- and six-coordinated to O atoms. The high coordination and the small number of dangling bonds of the (110) surface thus justify its low surface energy in β-PbO_2 as well as in other rutile metal oxides.[23,27,47,48] However, there are other factors, *e.g.*, bond contractions and surface electronic structure, that can jointly determine the actual surface energy of metal oxides.[49] We find that the fivefold-coordinated Pb atoms were slightly relaxed downward while the sixfold-coordinated Pb atoms were slightly relaxed upward. These relaxations cause ~0.20 Å downward shift of the surface plane with fivefold Pb atoms below the plane with sixfold Pb atoms, smaller than the reported value of ~0.42 Å for rutile VO_2 and TiO_2. This smaller downward shift coincides with a much larger atomic mass of Pb (207.2) compared to that of V (50.95) and Ti (47.87). Significant out-of-plane relaxations of ~ 0.24 Å are also observed for the in-plane O atoms (Fig. 1). The relaxed atomic structure of the (100), (101), (001), and (111) surfaces is also depicted in Fig. 1(b)–(e). The difference between unrelaxed and relaxed surface energies ($\Delta\gamma$) presented in Table 2 would reflect the overall relaxations of the atomic surface in the slab models.

To predict the thermodynamic equilibrium shape of the stoichiometric β-PbO_2 particle, the Wulff principles are employed.[44] The Wulff shape is constructed by minimizing the sum of the work of surface formation $A_{hkl}\gamma_{hkl}$, where A_{hkl} is the total area of the faces parallel to the (hkl) plane of the crystal. These faces are perpendicular to the vectors from the crystallization centre with the length (d_{hkl}) proportional to the surface energies.[28,50,51]

$$d_{hkl} \sim \gamma_{hkl}. \quad (5)$$

The facets corresponding to the low energy surface would comprise the equilibrium shape of the crystal. Fig. 2 shows the equilibrium shape of stoichiometric β-PbO_2 constructed based on the surface energies in Table 2. We find that only three of the five surfaces investigated here appear in the Wulff construction. Corresponding to its lowest surface energy, the (110) surface is the dominant facet in the crystal shape (45% of the total surface area). This result is analogous to rutile TiO_2, SnO_2, and VO_2 in which the (110) surface dominates the crystal shape. The other two facets that appear in the stoichiometric thermodynamic equilibrium shape are the (101) and (100) surfaces, consistent with their relatively low surface energies

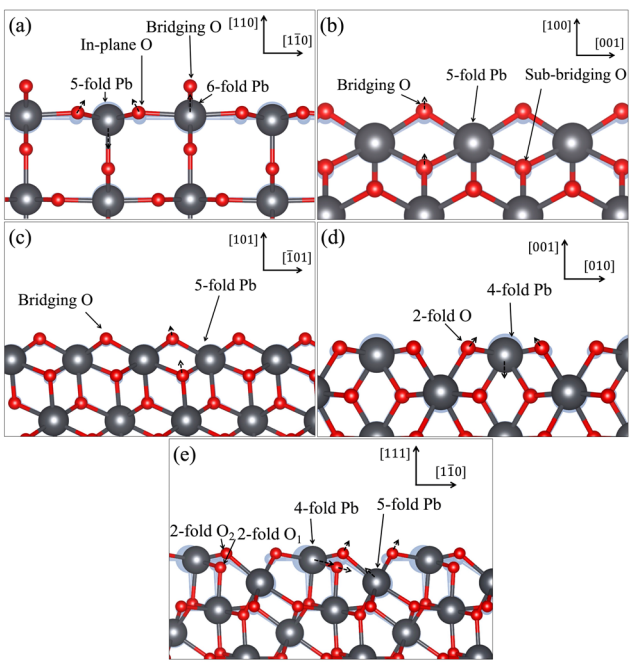

Fig. 1 Atomic structure of the β-PbO_2 relaxed (a) (110), (b) (100), (c) (001), (d) (101), and (e) (111) surfaces. The dashed arrows indicate the relaxing direction of the notated Pb and O ions. The unrelaxed atomic structure is also shown as a light-grey shadow.

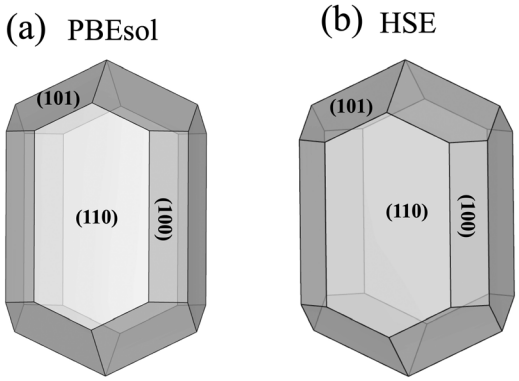

Fig. 2 Thermodynamic equilibrium shape of stoichiometric β-PbO_2 obtained by the Wulff construction using the (a) PBEsol and (b) HSE functional.

as shown in Table 2 (see Table 4 for the surface area fraction). It is, however, not always true that the low energy surfaces would appear in the equilibrium shape as in the case of VO_2 where the (100) surfaces are governed by (110) facets. Mellan *et al.* suggested that the (100) facet would be present in the Wulff when $\frac{\gamma_{110}}{\gamma_{100}} > \cos 45^\circ$ (the angle between these two planes is 45°).[27] In our case, the (100) facet appears in the Wulff shape because $\frac{\gamma_{110}}{\gamma_{100}} = 0.87 > \cos 45^\circ (0.77)$. This is analogous to the study in ref. 23 in which the thermodynamic stability of the surface $(h_1k_1l_1)$ with respect to the surface $(h_2k_2l_2)$ was determined based on the free-energy change on the formation of facets.

Experimentally, the crystal structure and morphology of β-PbO_2 have been often studied by scanning electron microscopy (SEM) and X-ray diffraction (XRD). The grain shape and crystallinity of β-PbO_2 can be diverse depending on the growth techniques and conditions such as anodizing current density and temperature. However, the crystal grain with an octahedral-like shape has been often observed in many growth processes.[4,7,9,12,52] In addition to transmission electron microscopy (TEM) which is frequently used to identify the preferred orientation of crystal growth, X-ray diffraction is another viable technique to identify the preferred orientation with a cheaper cost.[53,54] Many authors have often reported the scanning electron microscopy image (SEM) of crystal grains or crystal shapes without practical identification of the exposed facets. Our predicted equilibrium crystal shape of the stoichiometric β-PbO_2 (Fig. 2) is unlikely to represent the observed octahedral-like shape of the as-grown β-PbO_2 crystal. Several factors can be naturally considered as a cause of this inconsistency. For instance, the presence of impurities and defect formation in the vicinity of the surface can significantly change the free surface energy of the as-grown crystal as compared to the defect-free surface of β-PbO_2.[21,27,55] This may result in the modification of the equilibrium crystal shape as theoretically predicted in doped intermetallic compounds[56] and hydrogenated metal oxides.[57,58]

B. Non-stoichiometric surfaces

Naturally, point defects can form in the bulk during the growing processes of crystalline materials and, of course, can migrate or present in the vicinity of the surface of a crystal, resulting in a non-stoichiometric surface. Here, we investigate the energetics of the surface containing oxygen defects, *i.e.*, oxygen vacancy (reduced surface) and extra oxygen atoms adsorbed on the surface (oxidized surface). Not only the (110) surface but the other low Miller-index surfaces, *i.e.*, (100), (101), (001), and (111), are taken into account to ensure that the energetically favorable surfaces for a certain growth condition are realized. To simulate the reduced and oxidized surfaces, the non-stoichiometric slab supercells for the corresponding surfaces are created, and the surface free energies defined in eqn (3) corresponding to the Pb and O composition are then estimated to determine the relative thermodynamic stability. To estimate the surface free energy of a reduced/oxidized surface, the energy of an O_2 molecule is required, and the correction due to the GGA overbinding of the O_2 molecule is reportedly applied to the oxygen chemical potential in eqn (3). Our calculated O_2 binding energy in the triplet ground state based on the PBEsol of −6.66 eV is slightly more negative than the previously reported value whereas the calculated equilibrium O_2 bond length of 1.23 Å is identical.[27] Using the experimental O_2 binding energies at absolute zero of −5.12 eV,[59] the overbinding of the O_2 molecule based on our DFT-GGA calculations is thus estimated to be ∼1.54 eV. Half of this value (0.77 eV) is then used to correct non-stoichiometric surface energies defined in eqn (3).[60] It is worth noting that our calculations within the PBEsol yield the formation enthalpies of rutile tetravalent oxides including PbO_2, TiO_2, VO_2, and TiO_2 very close to the experimental values. The difference between theoretical and experimental values is less than 0.1 eV (Fig. S2 in ESI†). Some authors suggested that because of this very small shift, the overbinding of the O_2 molecule by the GGA calculations could be negligible.[27,61] The improvement of formation enthalpies of the oxides by the PBEsol over the conventional PBE likely resulted from the improved lattice constant of solids. However, the molecular atomization (binding) energies are not accurately given,[36] consistent with our calculated O_2 binding energy, which is more negative than the ones obtained by the conventional GGA.[27,60,61] The surface energies of non-stoichiometric β-PbO_2 with respect to both the corrected and as-received O_2 energy are included in Fig. 3 for comparison.

For the (110) surface, the 2 × 1 × 1 repetition of the stoichiometric slab is adopted to investigate the reduction and oxidation properties. To simulate the reduced (oxidized) surface, the oxygen atom(s) are symmetrically removed (added) on each side of the slab supercell, in such a way that the Pb and O atomic configuration on the surface is equivalent. This is to ensure that the dipole and spurious effects introduced by the amended surfaces are minimized. Due to the supercell size, only five values of N_O are allowed, if the adatoms or vacancies are confined within 1 monolayer (ML) of the supercell slab; $N_O = -1, -2$ correspond to partially and fully reduced surfaces and $N_O = 1, 2$ correspond to partially and fully oxidized surfaces (number of configurations is analogous to ref. 27 in which the redox behavior of the (110) surface of VO_2 was discussed). There are two possible ways to create an O vacancy on the (110) surface: removal of (i) the two coordinated bridging O atom or (ii) the three coordinated in-plane O atom. The formation energy of oxygen vacancies or adsorbed oxygen atoms on the surface can be defined as

$$E^f(D) = \frac{1}{2}[E_{slab}(\text{perfect}) - E_{slab}(D) - N_O E_{O_2}], \quad (6)$$

where E_{slab} (perfect) is the total energy of the stoichiometric slab supercell and $E_{slab}(D)$ is the total energy of the same supercell with oxygen vacancies or adsorbed oxygen atoms on the surface of the slab. $E^f(D)$ is calculated to be 0.49 eV for the bridging O vacancy and 1.56 eV for the in-plane O vacancy. This much higher stability (∼1 eV) of the bridging O vacancy with respect to the in-plane O vacancy was also reported for the

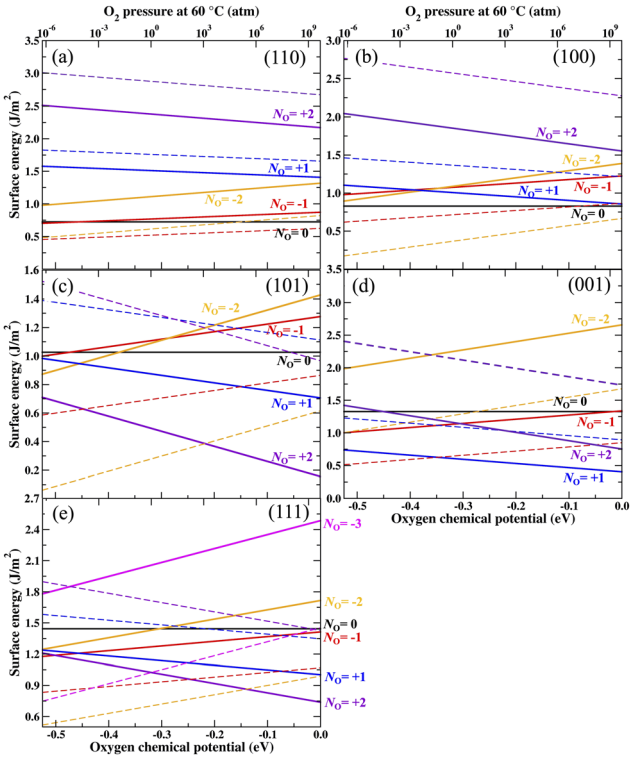

Fig. 3 Surface free energies of nonstoichiometric β-PbO_2 for (a) (110), (b) (100), (c) (101), (d) (001), and (e) (111) surfaces. The surface free energies without the correction due to O_2 overbinding are also included as dashed lines.

rutile VO_2 (110) surface. Removal of another bridging O from the partially reduced (110) surface with the bridging O vacancy results in a formation energy of 1.38 eV which is much lower than the formation energy caused by the removal of the in-plane O atom of 1.70 eV. It is therefore believed that only the bridging O vacancies can form in the partially and fully reduced (110) surface of PbO_2. The in-plane O vacancy, however, may form once all the bridging O are removed.

For the oxidized (110) surface, we first consider the case of partial oxidation (N_O = +1). An extra O atom can be added on the surface in two configurations: (i) vanadyl-like adsorption and (ii) bridging adsorption. The calculated formation energies of adsorbed oxygen on the surface are 2.14 eV and 2.35 eV for bridging and vanadyl-like adsorption, respectively. The positive formation energies indicate that the adsorption of the O atom on the (110) surface of PbO_2 is an endothermic process, unlike in VO_2 where O adsorption on the (110) surface is exothermic. This is likely because the V atom, which is a transition metal (group V) with unfilled d orbitals, can form more chemical bonds with O atoms compared to the Pb atom. We also investigate the possibility of the adsorption of two extra O atoms on the surface, forming a fully oxidized surface (N_O = +2) by considering total vanadyl-like, total bridging, monoperoxo, and bridging-peroxo configurations. The monoperoxo and bridging-peroxo configurations, however, cannot be stabilized against spontaneous O_2 formation, not involving in the surface vicinity. Hence, only total vanadyl-like and total bridging configurations are considered for a fully oxidized surface. The most energetically atomic configurations for each N_O of the non-stoichiometric (110) and the other low-index surfaces, *i.e.*, the (100), (101), (001), and (111) surfaces, are shown in ESI† (Fig. S3–S7).

The surface free energies of the possible reduced/oxidized (110) surface as a function of $\tilde{\mu}_O$ are shown in Fig. 3(a). The accessible range of $\tilde{\mu}_O$ is limited by the formation of gaseous O_2 (upper bound $\tilde{\mu}_O$ = 0, O-rich) and PbO (lower bound $\tilde{\mu}_O$= −0.53 eV, O-poor). To connect $\tilde{\mu}_O$ with the experimental access, we convert $\tilde{\mu}_O$ into pressure dependence at a fixed temperature of 60 °C, a typical temperature for growing PbO_2 thin films,[62] as depicted at the top *x*-axis of Fig. 3(a)–(d). For the surface free energies without the correction due to O_2 over-binding, it is shown in Fig. 3(a) that the completely reduced surface (N_O = −2) is the most thermodynamically stable surface for all range of accessible O_2 partial pressure. By contrast, with the correction, the perfect (110) surface is rather stable for most range of accessible O_2 partial pressure whereas the partially reduced surface becomes stable for very low O_2 partial pressure (10^{-6}–10^{-3} atm). These results show that the predicted relative stability of the non-stoichiometric surfaces with respect to the perfect surface depends on whether the correction is applied. The totally reduced, partially oxidized, and fully oxidized (110) surfaces are never energetically stable for the allowed range of $\tilde{\mu}_O$ regardless of the correction.

For the (100), (001), (101), and (111) surfaces, the procedure used for the (110) surface was adopted to realize the most energetically favorable configuration of the oxygen-related defects on the respective surfaces. The introduction of oxygen vacancies to create the reduced surfaces was limited by removal of either the topmost oxygen atoms with low coordination numbers, *i.e.*, the bridging oxygen atoms, or the two-fold oxygen atoms (Fig. 1). For the oxidized surfaces, additional oxygen atoms are assumed to initially lie near the surface Pb atoms mimicking the Pb coordination in the bulk-like region. The supercell created by 2 × 1 × 1 repetition of the stoichiometric slab was employed to investigate the redox properties of the (100) surface. Like the (110) surface, five values of N_O are allowed (N_O = −2, −1, 0, 1 and 2) because of the supercell size. The free surface energies of the non-stoichiometric (100) surface (Fig. 3(b)) show that the perfect surface is the most stable with respect to the non-stoichiometric surfaces for the entire range of allowed $\tilde{\mu}_O$. The partially (N_O = −1) and totally reduced surfaces (N_O = −2) are unstable for the entire range of allowed $\tilde{\mu}_O$; however, the totally reduced surface may form in the very reducing condition in which PbO begins to precipitate. The partially and fully oxidized (100) surfaces are also never stable, indicating that adding O atoms on the fivefold-coordinated Pb atom is unlikely.

The supercell identical to the stoichiometric slab of each respective surface was employed to investigate the redox properties of the (101), (001), and (111) surfaces, which allows the removal of up to two surface O atoms, corresponding to 1ML of vacancies. For the (101) surface, the removal of oxygen atoms

costs relatively high energy, resulting in thermodynamic instability of the reduced surface with respect to the stoichiometric surface for most range of allowed $\tilde{\mu}_O$. Nevertheless, the totally reduced (101) surface might be stable in very reducing conditions. On the other hand, our calculations suggest that the (101) surface can feasibly adsorb up to two extra O atoms which tend to form the O–O bonds with the surface O atoms (Fig. S5, ESI†). These O–O bonds would cause very low surface free energy of the fully oxidized (101) surface which becomes the most stable termination for the entire range of $\tilde{\mu}_O$ as shown in Fig. 3(c). For the (001) surface, we find that the partially reduced surface is lower in energy than the stoichiometric one for almost the entire range of allowed $\tilde{\mu}_O$. The totally reduced surface, however, has very high surface energy and is thus unstable. On the other hand, the partially oxidized (001) surface (N_O = +1), in which an extra O atom is strongly bonded to the two surface O atoms with an O–O bond length of ~1.47 Å, has very low surface energy, and becomes the most energetically stable termination for the non-stoichiometric (001) surface (Fig. S6, ESI†). It is possible to add one more extra O atom on top of the surface Pb atom, producing a fully oxidized surface (N_O = +2); however, its surface energy is higher than that of the partially oxidized surface (N_O = +1) likely because of the remaining O dangling bonds on the surface. The low symmetry of the (111) termination results in a large slab surface with many O atoms on the surface, allowing up to three O atoms to be removed to create vacancies. On the other hand, only up to two O atoms can be adsorbed to the (111) surface (Fig. S7, ESI†). It is found that the (111) surface prefers oxidation to reduction. The surface energies of the oxidized surfaces are much lower than the stoichiometric one for the whole range of $\tilde{\mu}_O$. This can be attributed to the formation of O–O bonds on the surface with the equilibrium bond lengths of 1.24–1.26 Å, comparable to that of isolated O_2. Fig. 3(e) shows that the fully oxidized surface is the most energetically favorable compared to all other terminations of the (111) surface. Although the reduced (111) surfaces have relatively high surface energy, the (111) surface with 1/3 ML of the vacancies (N_O = −1) is more energetically favorable than the stoichiometric surface for the entire range of allowed $\tilde{\mu}_O$ and might be stable in the very reducing condition. The partially oxidized (111) surfaces with 2/3 ML (N_O = −2) and 1ML (N_O = −3) of the vacancies have relatively high surface energies and, thus, are never stable for the entire range of allowed $\tilde{\mu}_O$.

It is worth noting that the above discussion is based on the surface free energy with the correction due to O_2 overbinding in the GGA-PBE. Without the correction, the most energetically favorable termination for each surface must be re-identified using the dashed lines included in Fig. 3. For instance, the reduced surfaces will be the most stable for the (110) and (100) surfaces for the entire range of allowed $\tilde{\mu}_O$ instead of the stoichiometric ones. The totally reduced (101) surface will be the most stable for the growth condition under the ambient condition instead of the fully oxidized surface. A similar behavior for the interchange of the most stable termination is also observed for the (001) and (111) surfaces. The interpretation of the calculated results, thus, must be carried out with care. In what follows, we will adopt surface free energies with the correction for the prediction of the Wulff shape and the discussion.

Using the surface free energies in Fig. 3, we now can predict more realistic equilibrium particle shapes of β-PbO_2 through the Wulff construction for the growth conditions of interest. Assuming a common growth temperature of 60 °C, the thermodynamic equilibrium shapes of non-stoichiometric β-PbO_2 under the O-poor, ambient, and O-rich conditions are depicted in Fig. 4. The surface free energies that are used to construct the Wulff shapes in Fig. 4 are tabulated in Table 3. It is clearly seen that considering the redox properties of the surfaces leads to significant transformation of the equilibrium Wulff shape with respect to the stoichiometric one (Fig. 2). To elucidate this transformation, we calculated the area fraction f^A_{hkl} of each symmetrically distinct facet of the Wulff shape, which is defined as[63]

$$f^A_{hkl} = \frac{A_{hkl}}{\sum A_{hkl}}, \tag{7}$$

where A_{hkl} is the total surface area of all facets in the symmetrical equivalent planes $\{hkl\}$ in the Wulff shape. Consequently, the weighted surface energy $\bar{\gamma}$ is given by

$$\bar{\gamma} = \sum_{\{hkl\}} \gamma_{hkl} f^A_{hkl}, \tag{8}$$

which can be used as a basis to compare with the experimentally determined surface energies for which only one value is usually reported. Here, the surface anisotropy is given by the following equation:[63]

$$\alpha_\gamma = \frac{\sqrt{\sum_{\{hkl\}} (\gamma_{hkl} - \bar{\gamma})^2 f^A_{hkl}}}{\bar{\gamma}}. \tag{9}$$

This definition can be inferred as a coefficient of distinction of surface energies that are normalized across a Wulff shape with different weighted surface energies. For instance, a Wulff shape that possesses only one surface termination would be perfectly

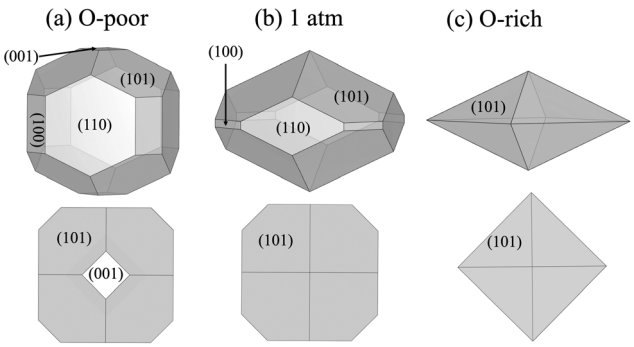

Fig. 4 Thermodynamic equilibrium shapes of non-stoichiometric β-PbO_2 obtained by the Wulff construction for (a) O-poor, (b) 1 atmospheric pressure, and (c) O-rich growth conditions with a growth temperature of 60 °C. The top views corresponding to each shape are shown in the bottom panel.

Table 3 Calculated surface energies for low-index surfaces of β-PbO_2 at a growth temperature of 60 °C for the O-poor, 1 atmospheric, and O-rich conditions

	γ (J m^{-2})		
Surface	O-poor	1 atm	O-rich
110	0.70	0.73	0.73
100	0.83	0.83	0.83
101	0.71	0.49	0.16
001	0.74	0.61	0.40
111	1.18	1.03	0.74

isotropic and α_γ = 0. From Table 4, it is seen that for the stoichiometric β-PbO_2, the {110} and {101} facets mostly contribute to the Wulff shape with the area fraction of 0.45 and 0.38, respectively, while under the ambient condition, the {101} facets are instead mostly exposed with an area fraction of 0.81.

Despite a significant shift of the exposed surfaces, the surface anisotropies between the stoichiometrically and ambient grown β-$PbO_2$are only slightly different. For the very reducing condition (O-poor), the Wulff shape is more isotropic with the main contribution from {101} followed by {110} planes, and minimal contributions from {100} and {001}. Interestingly, for the O-rich condition, the Wulff shape becomes perfectly isotropic; it is only exposed by {101} facets with very low weighted surface energy.

Based on our calculations, it is apparent that the {101} facets mostly contribute to the equilibrium Wulff shape in various growth conditions. This is consistent with several experimental results in which the substantial diffraction intensity of the (101) plane was observed in β-PbO_2 electrodes prepared by various methods. Recently, Chen *et al.* proposed a preparation method to control the crystal facet of the PbO_2 electrode.[10] It was found that employing specific surfactants can promote the formation of the low-index (101) facet and limit the formation of the high-index (211) facet. The pyramidal shape of the crystallite was clearly observed, which is in good agreement with our predicted Wulff shape for the O-rich condition shown in Fig. 4(c). In such case, the facet control using surfactants appeared to influence the facet formation and thereby replicate the O-rich growth condition. In addition, it was reported that at low plating temperatures one of the main XRD peaks of the β-PbO_2 samples is the (101) plane whereas at 30 °C the (110) plane is nearly inhibited.[4] The octahedral shape, which is virtually similar to the pyramid, was also observed in many well-formed grains in the samples of these authors. Besides, pyramidal-shape grains in various sizes were observed in the β-PbO_2 electrodes prepared by electrochemical deposition and modified with polyvinyl alcohol (PVA).[9] The XRD patterns showed comparable diffraction intensities of (110) and (101) planes in some samples and increased intensity of the (101) plane in the sample with 2% volume fraction of PVA, indicating the preferred orientation along these planes. Note that the XRD intensity of the (211) plane was also dominant in some samples. However, the high Miller-index surfaces usually have high surface energy and may not appear in the equilibrium Wulff shape. Last but not least the dominance of XRD intensity of the (101) plane and the pyramidal shape of β-PbO_2 grains prepared by electrodeposition were also reported earlier.[7] To our knowledge, neither the experimental surface energy nor anisotropy of the β-PbO_2 crystallites has been reported so far.

Table 4 The surface area fraction of distinct facets of β-PbO_2 under thermal equilibrium for the stoichiometric and the O-poor, ambient, and O-rich conditions at a growth temperature of 60 °C. The weighted surface energy ($\bar{\gamma}$) and surface energy anisotropy (α_γ) are also presented

	Area fraction			
Surface	Stoichiometric	O-poor	1 atm	O-rich
110	0.45	0.37	0.17	—
100	0.17	0.09	0.02	—
101	0.38	0.51	0.81	1.00
001	—	0.03	—	—
$\bar{\gamma}$ (eV)	0.86	0.72	0.54	0.16
α_γ	0.16	0.05	0.18	0.00

4. Conclusions

We have theoretically investigated the surface properties of β-PbO_2 using density-functional calculations based on the PBEsol functional. Our calculations show that for stoichiometric β-PbO_2, the surface energies of the low Miller-index planes are (110) < (100) < (101) < (001) < (111) consistent with the coordination numbers of surface atomic Pb and O. Using the calculated surface energies, we provide the equilibrium shape of stoichiometric β-PbO_2 through the Wulff construction. The (110) and (101) surfaces almost equally dominate the Wulff shape covering up to 83% of the surface area while the (111) surface does not appear in the shape. Calculations of the surface energies as a function of oxygen partial pressure show that most surfaces except for (100) and (110) are likely to be oxidized. Our results indicate that the growth conditions or the chemical environment that causes non-stoichiometry of the surface could modify the equilibrium Wulff shape of β-PbO_2. The oxidized (101) surface has much lower surface energy than the (110) surface. This results in the dominance of the (110) surface in the Wulff shape, contributing up to 81% and 100% under ambient and O-rich conditions, respectively.

Our predicted Wulff shapes and dominant facets are in good agreement with the experiments in which the pyramidal shape of the β-PbO_2 grains has often been observed with the (101) preferred orientation. Our results reveal that it is important to include the effects of the surface redox properties in the prediction of the morphology of a crystal. Controlling the exposed surface area of some facets could be beneficial for expanding the capability of PbO_2 electrodes.

Conflicts of interest

There are no conflicts to declare.

Acknowledgements

This work was supported by the Thailand Research Fund (Grant No. RSA6280068). A. N. acknowledges the Institute for Promotion of Science and Technology (DPST scholarship). P. R. wishes to thank T. Maluangnont for the useful discussion. We wish to thank NSTDA Supercomputer Center (ThaiSC) for providing computing resources for this work.

References

1 S. G. Kumar and K. S. R. K. Rao, *Appl. Surf. Sci.*, 2017, **391**, 124–148.
2 N. Barsan, D. Koziej and U. Weimar, *Sens. Actuators, B*, 2007, **121**, 18–35.
3 Y.-m Zhang, Y. Peng, X.-l Yin, Z.-h Liu and G. Li, *J. Chem. Technol. Biotechnol.*, 2014, **89**, 1954–1960.
4 B. Du, Z. Chen, Q. Yu, W. Zhu, W. Yan and Z. Guo, *Surf. Eng.*, 2018, **34**, 689–696.
5 A. Walsh, A. B. Kehoe, D. J. Temple, G. W. Watson and D. O. Scanlon, *Chem. Commun.*, 2013, **49**, 448–450.
6 C. G. Poll and D. J. Payne, *Electrochim. Acta*, 2015, **156**, 283–288.
7 J. Kong, S. Shi, L. Kong, X. Zhu and J. Ni, *Electrochim. Acta*, 2007, **53**, 2048–2054.
8 N. Yu, L. Gao, S. Zhao and Z. Wang, *Electrochim. Acta*, 2009, **54**, 3835–3841.
9 X. Li, H. Xu and W. Yan, *RSC Adv.*, 2016, **6**, 82024–82032.
10 X. Chen, C. Sun, C. Ma, H. Zhang, L. Cao and J. Yang, *J. Electroanal. Chem.*, 2021, **890**, 115246.
11 Q. Dai, J. Zhou, M. Weng, X. Luo, D. Feng and J. Chen, *Sep. Purif. Technol.*, 2016, **166**, 109–116.
12 J. Zhao, C. Zhu, J. Lu, C. Hu, S. Peng and T. Chen, *Electrochim. Acta*, 2014, **118**, 169–175.
13 N. Yu and L. Gao, *Electrochem. Commun.*, 2009, **11**, 220–222.
14 D. O. Scanlon, A. B. Kehoe, G. W. Watson, M. O. Jones, W. I. F. David, D. J. Payne, R. G. Egdell, P. P. Edwards and A. Walsh, *Phys. Rev. Lett.*, 2011, **107**, 246402.
15 G. Liu, J. C. Yu, G. Q. Lu and H.-M. Cheng, *Chem. Commun.*, 2011, **47**, 6763–6783.
16 X. Peng, L. Manna, W. Yang, J. Wickham, E. Scher, A. Kadavanich and A. P. Alivisatos, *Nature*, 2000, **404**, 59–61.
17 D. Zhou and L. Gao, *Electrochim. Acta*, 2007, **53**, 2060–2064.
18 G. Darabizad, M. S. Rahmanifar, M. F. Mousavi and A. Pendashteh, *Mater. Chem. Phys.*, 2015, **156**, 121–128.
19 F. Fu, W. Yang and C. Ke, *Mater. Chem. Phys.*, 2018, **220**, 155–160.
20 Z. He, M. D. Hayat, X. Yuan, X. Wang and P. Cao, *J. Appl. Electrochem.*, 2018, **48**, 783–791.
21 K. Reuter and M. Scheffler, *Phys. Rev. B: Condens. Matter Mater. Phys.*, 2001, **65**, 035406.
22 A. Soon, M. Todorova, B. Delley and C. Stampfl, *Phys. Rev. B: Condens. Matter Mater. Phys.*, 2007, **75**, 125420.
23 M. Ramamoorthy, D. Vanderbilt and R. D. King-Smith, *Phys. Rev. B: Condens. Matter Mater. Phys.*, 1994, **49**, 16721–16727.
24 D.-P. Song, Y.-C. Liang, M.-J. Chen and Q.-S. Bai, *Appl. Surf. Sci.*, 2009, **255**, 5702–5708.
25 A. Kiejna, T. Pabisiak and S. W. Gao, *J. Phys.: Condens. Matter*, 2006, **18**, 4207–4217.
26 A. Beltrán, J. Andrés, J. R. Sambrano and E. Longo, *J. Phys. Chem. A*, 2008, **112**, 8943–8952.
27 T. A. Mellan and R. Grau-Crespo, *J. Chem. Phys.*, 2012, **137**, 154706.
28 F. Jiang, L. Yang, D. Zhou, G. He, J. Zhou, F. Wang and Z.-G. Chen, *Appl. Surf. Sci.*, 2018, **436**, 989–994.
29 M. Heinemann, H. J. Terpstra, C. Haas and R. A. de Groot, *Phys. Rev. B: Condens. Matter Mater. Phys.*, 1995, **52**, 11740–11743.
30 S. Mahatara and B. Kiefer, *J. Phys.: Condens. Matter*, 2020, **32**, 255504.
31 R.-W. Zhang, C.-C. Liu, D.-S. Ma, M. Wang and Y. Yao, *Phys. Rev. B*, 2018, **98**, 035144.
32 R. Ahuja, A. Blomqvist, P. Larsson, P. Pyykkö and P. Zaleski-Ejgierd, *Phys. Rev. Lett.*, 2011, **106**, 018301.
33 D. H. M. Azevedo, G. S. L. Fabris, J. R. Sambrano and J. M. M. Cordeiro, *Comput. Mater. Sci.*, 2020, **171**, 109222.
34 G. Gibson, A. Morgan, P. Hu and W.-F. Lin, *Chem. Phys. Lett.*, 2016, **654**, 46–51.
35 G. S. L. Fabris, D. H. M. Azevedo, A. C. Alves, C. A. Paskocimas, J. R. Sambrano and J. M. M. Cordeiro, *Phys. E*, 2021, 115037.
36 J. P. Perdew, A. Ruzsinszky, G. I. Csonka, O. A. Vydrov, G. E. Scuseria, L. A. Constantin, X. Zhou and K. Burke, *Phys. Rev. Lett.*, 2008, **100**, 136406.
37 P. E. Blöchl, *Phys. Rev. B: Condens. Matter Mater. Phys.*, 1994, **50**, 17953.
38 G. Kresse and J. Furthmüller, *Comput. Mater. Sci.*, 1996, **6**, 15–50.
39 H. J. Monkhorst and J. D. Pack, *Phys. Rev. B: Solid State*, 1976, **13**, 5188.
40 D. J. Payne, G. Paolicelli, F. Offi, G. Panaccione, P. Lacovig, G. Beamson, A. Fondacaro, G. Monaco, G. Vanko and R. G. Egdell, *J. Electron Spectrosc. Relat. Phenom.*, 2009, **169**, 26–34.
41 J. Heyd, G. E. Scuseria and M. Ernzerhof, *J. Chem. Phys.*, 2003, **118**, 8207–8215.
42 W.-X. Li, C. Stampfl and M. Scheffler, *Phys. Rev. B: Condens. Matter Mater. Phys.*, 2003, **68**, 165412.
43 T. Wang, S. Wang, Q. Luo, Y.-W. Li, J. Wang, M. Beller and H. Jiao, *J. Phys. Chem. C*, 2014, **118**, 4181–4188.
44 G. Wulff, *Z. Kristallogr. - Cryst. Mater.*, 1901, **34**, 449–530.
45 N. Martsinovich, D. R. Jones and A. Troisi, *J. Phys. Chem. C*, 2010, **114**, 22659–22670.
46 F. Labat, P. Baranek and C. Adamo, *J. Chem. Theory Comput.*, 2008, **4**, 341–352.
47 J. Oviedo and M. J. Gillan, *Surf. Sci.*, 2000, **463**, 93–101.
48 H. Perron, C. Domain, J. Roques, R. Drot, E. Simoni and H. Catalette, *Theor. Chem. Acc.*, 2007, **117**, 565–574.
49 M. Sterrer and H.-J. Freund, *Surface and Interface Science*, 2013, pp. 229–278.
50 P. Marcus, É. Protopopoff and V. Maurice, in *Mechanics – Microstructure – Corrosion Coupling*, ed. C. Blanc and I. Aubert, Elsevier, 2019, pp. 91–120.
51 G. D. Barmparis and I. N. Remediakis, *Phys. Rev. B: Condens. Matter Mater. Phys.*, 2012, **86**, 085457.
52 T. T. T. Mai, T. B. Phan, T. T. Pham and H. H. Vu, *Adv. Nat. Sci.: Nanosci. Nanotechnol.*, 2014, **5**, 025004.
53 L. Zhang, A. A. S. Gonçalves and M. Jaroniec, *RSC Adv.*, 2020, **10**, 5585–5589.

54 Y. Bi, S. Ouyang, N. Umezawa, J. Cao and J. Ye, *J. Am. Chem. Soc.*, 2011, **133**, 6490–6492.
55 X. G. Wang, W. Weiss, S. K. Shaikhutdinov, M. Ritter, M. Petersen, F. Wagner, R. Schlögl and M. Scheffler, *Phys. Rev. Lett.*, 1998, **81**, 1038–1041.
56 H.-Y. Wang, X.-N. Xue, X.-Y. Xu, C. Wang, L. Chen and Q.-C. Jiang, *CrystEngComm*, 2016, **18**, 8599–8607.
57 T. Xia and X. Chen, *J. Mater. Chem. A*, 2013, **1** 2983–2989.
58 M. Zhang, W. Wang and Y. Chen, *Appl. Surf. Sci.*, 2018, **434**, 1344–1352.
59 D. R. Lide, *CRC Handbook of Chemistry and Physics*, CRC press, Boca, 2004.
60 D. Santos-Carballal, A. Roldan, R. Grau-Crespo and N. H. de Leeuw, *Phys. Chem. Chem. Phys.*, 2014, **16**, 21082–21097.
61 L. Wang, T. Maxisch and G. Ceder, *Phys. Rev. B: Condens. Matter Mater. Phys.*, 2006, **73**, 195107.
62 D. J. Payne, R. G. Egdell, D. S. L. Law, P.-A. Glans, T. Learmonth, K. E. Smith, J. Guo, A. Walsh and G. W. Watson, *J. Mater. Chem.*, 2007, **17**, 267–277.
63 R. Tran, Z. Xu, B. Radhakrishnan, D. Winston, W. Sun, K. A. Persson and S. P. Ong, *Sci. Data*, 2016, **3**, 160080.
64 M. Binnewies and E. Milke, *Thermochemical data of elements and compounds*, Wiley Online Library, 2002.
65 R. Hill, *Acta Crystallogr., Sect. C: Cryst. Struct. Commun.*, 1985, **41**, 1281–1284.

